TOWARD A HIGH RESOLUTION REAL GAS FINITE VOLUME SOLVER WITH MULTI OPTIMAL ORDER DETECTION

Michael Deligant[1*], Xesús Nogueira[2], Sofiane Khelladi[1], Emilie Sauret[3], Brian Reding[4]

[1] DynFluid laboratory, Métiers ParisTech
151 boulevard de l'Hopital,75013 Paris, France
michael.deligant@ensam.eu

[2] Group of Numerical Methods in Engineering, Universidade da Coruña, Campus de Elviña, 15071, A Coruña, Spain

[3] Queensland University of Technology,
Brisbane, Queensland, Australia

[4] Universidad Complutense, Departamento de Estructura de la Materia, Física Térmica y Electrónica, Madrid, Spain

* Corresponding Author

ABSTRACT

The accurate predictions of the ORC expander performance rely on validated numerical tools that take into account the full complexity of the underlying physics. The expansion of organic vapor in turbomachines rotor and stator features non-ideal gas behavior with chocked flow in transonic conditions and supersonic expansion. In this paper, a finite volume solver using moving least squares approximations for higher order reconstruction is used. The real gas properties are taken into account using lookup tables with Tabular Taylor Series Expansion. The SLAU approximate Riemann solver is used for its compatibility with real gas computations. The conventional/classical slope limiter approach to handle shocks is replaced with the a posteriori paradigm for the local order reduction (MOOD). The developments are validated by comparing available solution of supersonic expansion of R245fa in a converging diverging nozzle test case.Further developments will focus on the CFD of turbulent non ideal dense gas expansions with implicit large eddy scale techniques using MOOD and automatic dissipation adjustment (ADA) for turbomachinery applications.

1. INTRODUCTION

Organic Rankine cycle allow the conversion of medium to low grade heat into power. Although the principle of ORC is known for decades, the increases of electricity cost, the climate crisis, the development of efficient working fluids and the maturity of the expanders technologies helped its development and commercial deployment Tartière and Astolfi (2017). The ORC expander is the key part of the plant. The optimization of its performance at design stage is crucial. The use of dense organic vapor as working fluid with high molecular complexity needs to be taken into account in the models used for the design and performance predictions of the expander Spinelli et al. (2017). The real gas properties and behavior can be taken into account using adapted equations of state such as Peng-Robinson or Redlich-Kwong Sauret and Gu (2014) or Look-up table interpolation such as the work of Pini et al. (2015); Rubino et al. (2018).

Unstructured finite volume solver are well suited for the simulations of complex geometries of industrial interest, such as ORC expanders. To obtain a given accuracy of the results, the number of mesh cells needs to be increased for a given spatial order, or the spatial order need to be increased for a given

mesh.

In this study, a finite volume solver using moving least squares approximation for the high order reconstruction is considered. The solver is adapted to take into account real gas properties using look-up table and Taylor tabular series expansions.

2. GOVERNING EQUATIONS

The Inviscid compressible Euler equations read as

$$\frac{\partial \mathbf{U}}{\partial t} + \frac{\partial \mathbf{F}_x(\mathbf{U})}{\partial x} + \frac{\partial \mathbf{F}_y(\mathbf{U})}{\partial y} = 0 \tag{1}$$

where $\mathbf{U} = \begin{pmatrix} \rho \\ \rho u \\ \rho v \\ \rho E \end{pmatrix}$, $\mathbf{F}_x(\mathbf{U}) = \begin{pmatrix} \rho u \\ \rho u^2 + p \\ \rho uv \\ (\rho E + p)u \end{pmatrix}$ and $\mathbf{F}_y(\mathbf{U}) = \begin{pmatrix} \rho v \\ \rho uv \\ \rho v^2 + p \\ (\rho E + p)v \end{pmatrix}$.

3. FINITE VOLUME SOLVER

Equations (1) can be written in integral form as

$$\int_{\Omega_I} \frac{\partial \boldsymbol{U}}{\partial t}\, d\Omega + \int_{\Gamma_I} \boldsymbol{\mathcal{F}} \cdot \boldsymbol{n}\, d\Gamma = \mathbf{0} \tag{2}$$

where Ω_I is the volume of the control volume, Γ_I is the area of the control volume cells and $\boldsymbol{n} = (n_x, n_y)^T$ is the unitary exterior normal of the contour and $\boldsymbol{\mathcal{F}} = (F_x, F_y)$ is the convective flux vector.

As it is usual in the finite volume approach, the integral over Γ_I is performed over the edges between two adjacent control volumes, so the value of the function $\boldsymbol{U}$ at the integration points on the interface must be reconstructed. An usual approach is using Taylor's polynomials Cueto-Felgueroso et al. (2007); Khelladi et al. (2011).

Introducing the approximated function $\boldsymbol{U}^h$ in equation (2) we obtain

$$\int_{\Omega_I} \frac{\partial \boldsymbol{U}^h}{\partial t}\, d\Omega + \int_{\Gamma_I} \boldsymbol{\mathcal{F}}^h \cdot \boldsymbol{n}\, d\Gamma = \mathbf{0} \tag{3}$$

where the superindex *h* indicates that the flux is computed with the reconstructed function at edges.

4. MOVING LEAST SQUARES APPROXIMATIONS

In the present work, high-order is achieved by using Taylor expansions and using Moving Least Squares (MLS) approximations for the computations of the derivatives. This approach is extensively described in Cueto-Felgueroso et al. (2006, 2007); Khelladi et al. (2011); Nogueira et al. (2010, 2016). Here we only introduce a brief description of the computation procedure.

In brief, a Moving Least Squares approximation of a function Φ belongs to the subspace spanned by a set of *basis functions* $\{N_I(\boldsymbol{x})\}$ associated to the nodes, such that it is given by

$$\boldsymbol{\Phi}^{MLS}(\boldsymbol{x}) = \sum_{j=1}^{n_{\boldsymbol{x}}} N_j(\boldsymbol{x}) \boldsymbol{\Phi}_j \tag{4}$$

which states that the approximation at a point $\boldsymbol{x}$ is computed using certain $n_{\boldsymbol{x}}$ surrounding nodes. This set of nodes is referred to as the *stencil* associated to the evaluation point $\boldsymbol{x}$. The number of nodes of the stencil depends on the order of the reconstruction Cueto-Felgueroso et al. (2007); Khelladi et al. (2011); Nogueira et al. (2016).

In equation (4) $N_j(\boldsymbol{x})$ are the MLS shape functions. To compute them, we define a m-dimensional basis, which in this case is defined as a polynomial basis (eq (5)).

$$\boldsymbol{p}^T(\boldsymbol{x}) = (1, x, y, z, x^2, y^2, z^2, xy, \ldots) \in \mathbb{R}^m \tag{5}$$

The dimension of the basis, m, determines the minimum number of points of the stencil. However, for stability reasons, this minimum number should be increased. In this work we use a value of $n_{\boldsymbol{x}} = 20$.

Then, the MLS-shape functions are defined as

$$\boldsymbol{N}^T(\boldsymbol{x}) = \boldsymbol{p}^T(\boldsymbol{x})\boldsymbol{M}^{-1}(\boldsymbol{x})\boldsymbol{P}(\boldsymbol{x})\boldsymbol{W}(\boldsymbol{x}) \tag{6}$$

where $\boldsymbol{P} = [\boldsymbol{p}^T(\boldsymbol{x_j})]_j$, is a $m \times n_{\boldsymbol{x}}$ matrix where the basis functions are evaluated at each point of the stencil, and $\boldsymbol{M}(\boldsymbol{x})$ is the $m \times m$ moment matrix given by

$$\boldsymbol{M}(\boldsymbol{x}) = \boldsymbol{P}(\boldsymbol{x})\boldsymbol{W}(\boldsymbol{x})\boldsymbol{P}^T(\boldsymbol{x}) \tag{7}$$

The kernel function $\boldsymbol{W}$ determines the properties of the scheme, required in the computation of $\boldsymbol{N}^T(\boldsymbol{x})$. We have chosen to use an exponential kernel Nogueira et al. (2010), defined as :

$$W(x, x^*, \kappa_x) = \frac{e^{-\left(\frac{s}{2c}\right)^2} - e^{-\kappa^2}}{1 - e^{-\kappa^2}} \tag{8}$$

with $s = \left|x_j - x^*\right|$, $d_m = max\left(\left|x_j - x^*\right|\right)$, with $j = 1, \ldots, n_{x^*}$, $c = \frac{d_m}{\kappa}$, x is the position of every cell centroid of the stencil and κ is a shape parameter, which is this work is taken as $\kappa = 6$. Moreover, x^* refers to the position of the point where the MLS shape function is evaluated.

In order to reconstruct the variable at integration points, we use Taylor series expansions. Thus, to define a quadratic reconstruction inside cell I, we require the computation of first and second derivatives

$$\boldsymbol{U}_I^{hb}(\boldsymbol{x}) = \boldsymbol{U}_I^h + \nabla \boldsymbol{U}_I^h \cdot (\boldsymbol{x} - \boldsymbol{x}_I) + \frac{1}{2}(\boldsymbol{x} - \boldsymbol{x}_I)^T \boldsymbol{H}^h \ (\boldsymbol{x} - \boldsymbol{x}_I) \tag{9}$$

These derivatives are computed at the cell centroids using MLS, from the derivatives of the shape functions as follows

$$\nabla \boldsymbol{\Phi}^{MLS}(\boldsymbol{x}) = \sum_{j=1}^{n_{\boldsymbol{x}}} \nabla \boldsymbol{N}_j(\boldsymbol{x})\boldsymbol{\Phi}_j \tag{10}$$

We refer the reader to Cueto-Felgueroso et al. (2007); Khelladi et al. (2011) for complete description of the computation of the derivatives using MLS.

5. RIEMANN SOLVER FOR REAL GAS

Equation (2) can be written in semi-discrete form as

$$\int_{\Omega_I} \frac{\partial \boldsymbol{U}}{\partial t} d\Omega + \int_{\Gamma_I} \boldsymbol{\Theta}(\boldsymbol{U}^{hb+}, \boldsymbol{U}^{hb-})\, d\Gamma + \int_{\Gamma_I} \boldsymbol{\mathcal{F}}^V \cdot \boldsymbol{n}\, d\Gamma = \boldsymbol{0} \tag{11}$$

where $\boldsymbol{\Theta}(\boldsymbol{U}^{hb+}, \boldsymbol{U}^{hb-})$ is a suitable numerical flux, and + and − refers to the left and right Riemann states of the cell I.

In this work, Simple Low-dissipation AUSM Riemann solver from Shima and Kitamura (2009) is used. The time integration is achieved using an explicit 2nd order 4 stages Runge Kutta solver.

6. MULTI OPTIMAL ORDER DETECTION

Using a high-order scheme for the discretization of equation (1) requires the use of any stabilization scheme to keep the stability of the scheme Michalak and Ollivier-Gooch (2008). In this work, we propose to use the Multi-dimensional Optimal Order Detection (MOOD) approach Clain et al. (2011); Diot et al. (2012) for the automatic local adaptation of the reconstruction order, granting the stability of the numerical scheme.

The main idea of this approach is to compute, each step of the time integration algorithm, the cell averaged values using the most accurate available scheme. This solution is called candidate solution. Since this solution is obtained using a high-order method, it is possibly oscillating or even not physical, if negative densities and pressures appear in the solution. If this happens, this solution is not valid, which in this context means that it gives some negative densities and pressures, or that the level of nonphysical oscillations is high. A set of criteria is defined to determine if the candidate solution is valid or not. In Clain et al. (2011) an iterative scheme was proposed for reducing progressively and locally the order of the numerical scheme, recomputing the solution and evaluating again if the solution is not admissible. This evaluation/order reduction procedure is performed until the solution is considered admissible or the numerical scheme reaches first-order, which always gives admissible solutions. This procedure is called MOOD Clain et al. (2011); Diot et al. (2012). It is worth to remark that, differently than most of the usual procedures for stabilization, the detection of the troubled cells is performed *a posteriori*, that is, once it is known the exact cells where the numerical scheme is compromised to obtain an admissible solution. The procedure is as follows. Once the candidate solution is computed each Runge-Kutta step, the following chain of detectors is used

Physical Admissible Detector (PAD) Clain et al. (2011): Checks if the candidate solution has positive density and pressure. Thus, if the candidate solution has negative values of pressure and/or density in a cell, or even a `NaN` value, this cell is marked as not valid and is recomputed again using a lower order scheme.

Numerical Admissible Detector (NAD) Dumbser and Diot (2014): It is a relaxed version of the Discrete Maximum Principle (DMP)Clain et al. (2011). It checks if the solution is monotonic and new local extrema are not created.

$$\min_{\mathbf{y}\in\mathcal{V}_i}\left(\mathbf{U}^n(\mathbf{y})\right) - \delta \leqslant \mathbf{U}^*(\mathbf{x}) \leqslant \max_{\mathbf{y}\in\mathcal{V}_i}\left(\mathbf{U}^n(\mathbf{y})\right) + \delta \tag{12}$$

In equation (12) superscript n indicates the previous Runge-Kutta step, and superscript * refers to the candidate solution. The δ parameter allows a certain level of oscillations. Here we use the values proposed in Dumbser and Diot (2014)

$$\delta = \max\left(10^{-4}, 10^{-3}\cdot\left(\max_{\mathbf{y}\in\mathcal{V}_i}\left(\mathbf{U}^n(\mathbf{y})\right) - \min_{\mathbf{y}\in\mathcal{V}_i}\left(\mathbf{U}^n(\mathbf{y})\right)\right)\right) \tag{13}$$

Note that in order to work with this *a posteriori* formulation, all the variables in equation (13) should be normalized with an adequate reference value to get a value between 0 and 1. In the original formulation Clain et al. (2011); Diot et al. (2012); Dumbser and Diot (2014) the set $\mathcal{V}_i$ represents the set of first neighbors of the point $\mathbf{x}$. In this work the values are normalized by dividing by the maximum value in

the stencil used by MLS approximations.This is based on the ideas presented in Tsoutsanis (2018) in the context of slope limiters. The fulfillment of the NAD condition implies that the candidate value remains between the local minimum and the local maximum of the previous time step. In all of the examples of this work, the NAD is checked in the density. It is possible to check in the full vector of conservative variables as suggested by Diot et al. (2012).

7. REAL GAS PROPERTIES USING LOOK-UP TABLE

The real gas properties of the fluids are computed using Tabular Taylor Series Expansion (TTSE) as presented for water in Miyagawa and Hill (2002). The variable of interest z is computed from the values of variables x and y (eq 14).

$$z = z_{i,j} + \Delta x \left(\frac{\partial z}{\partial x}\right)_y + \Delta y \left(\frac{\partial z}{\partial y}\right)_x + \frac{1}{2}\Delta x^2 \left(\frac{\partial^2 z}{\partial x^2}\right)_y + \frac{1}{2}\Delta y^2 \left(\frac{\partial^2 z}{\partial y^2}\right)_y + \Delta x \Delta y \left(\frac{\partial^2 z}{\partial y \partial x}\right) \tag{14}$$

With $\Delta x = x - x_i$ and $\Delta x = y - y_j$.

$x \in [x_{min}, x_{max}]$ and $x_i = x_{min} + i * dx$ with $dx = \frac{x_{max} - x_{min}}{N}$.

$y \in [y_{min}, y_{max}]$ and $y_j = y_{min} + j * dy$ with $dy = \frac{y_{max} - y_{min}}{N}$

In order to avoid mapping the mixture area, the value of y_{min} is replaced by the corresponding value on the saturation vapor curve. Thus $y_i = y_{sat}(x) + j * dy$. For internal energy versus density with R245fa, $y_{sat}(x)$ is approximated by a 5th order polynomial (see fig. 1).

The thermodynamic domain is meshed with constant intervals. Given a point (x, y), the determination of the closest point (x_i, y_i) is then straightforward.

The thermodynamic tables are generated using the CoolProp library from Bell et al. (2014) which is based on the Helmholtz Energy equation of state. The derivative can be computed using finite difference approximations.

Tables based on internal energy and density are built to interpolate pressure, temperature and speed of sound using CoolProp. For the boundary conditions and initial values, tables based on pressure and temperature are generated to compute the density and internal energy.

Although this step might be long if a high number of points is required, this is done only once for a given domain of interest. The values of the tables are stored in a binary files that can be reloaded for further simulations. For this study each thermodynamic grid has 250 x 250 elements, which requires only 3 Mo of memory each.

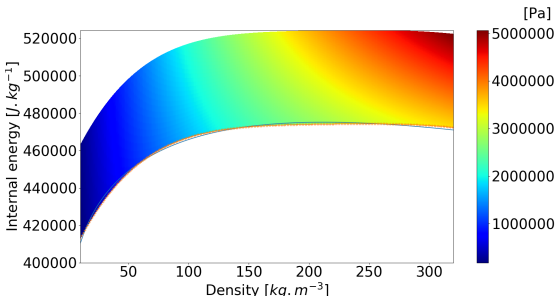

Figure 1: R245fa pressure versus density and internal energy, Vapor saturation curve (blue line), Polynomial saturation curve (cross)

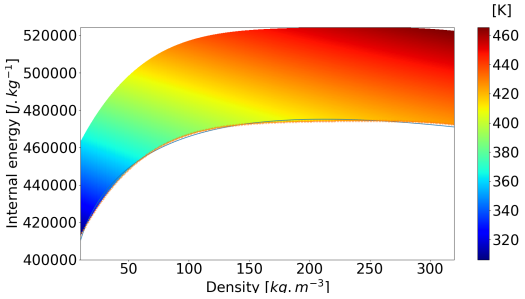

Figure 2: R245fa temperature versus density and internal energy

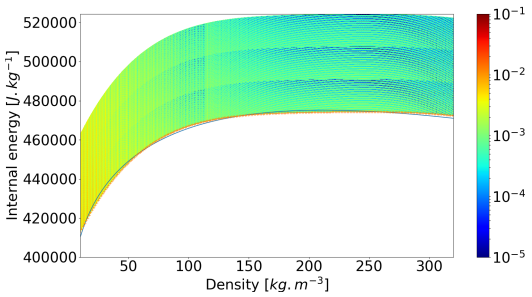

Figure 3: Relative error on R245fa pressure versus density and internal energy

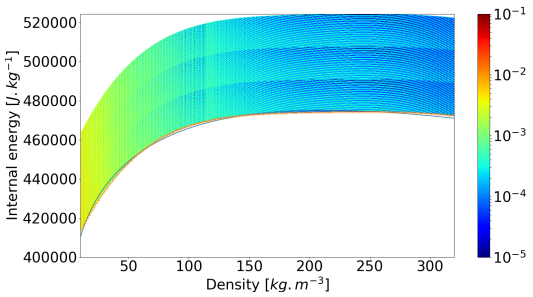

Figure 4: Relative error on R245fa temperature versus density and internal energy

8. RESULTS AND DISCUSSIONS

The simulations are carried out on the nozzle designed for R245fa proposed in Spinelli et al. (2013). The inlet pressure is 3.7 MPa, with an inlet temperature of 432.35 K and an inlet velocity of 12.6 $m.s^{-1}$. The outlet pressure is set to 0.2 MPa. As the outlet reach supersonic condition, the outlet boundary condition is actually interpolated from the inside domain. On the walls a slip condition is considered. The computing domain is initialized with the values of the inlet condition.

The parameters of the look-up table generated are presented in table 1. The pressure map and temperature map on the domain of interest are presetend in figures 1 and 2 with the associated relative error in figures 3 and 4.

Table 1: Look-up tables parameters

	min	max	Tables
Density	10	320	Pressure, Temperature, Speed of sound
Internal energy	400000	500000	
Presure	0.1	4.5	Density, Internal Energy
Temperature	300	550	

The geometry of the nozzle with associated mesh is presented in figure 5. The non dimensional base size of the triangular unstructured mesh is 0.2.

The computations are run until steady state. During transient operation, the MOOD locally reduces the reconstruction order preventing the oscillations and the divergence of the solution. At the end of the computation, the order reduction concerns only some cells in the diverging part of the nozzle located next to the walls.

The stationary field for Mach number, pressure and temperature are presented in figures 6, 7 and 8. The evolution of the pressure along the nozzle axis is presented in figure 9. Although there are some small differences with the reference curve from Spinelli et al. (2013), a fairly good agreement is obtained. Similarly, the Mach number along the nozzle axis is presented in figure 10. The difference seems more significant, especially in the diverging part. The differences might be explained by the fact that the reference curve were obtained using a real gas 1D simulation. In the present study, using 2D simulations, the results are not totally homogeneous in the sections, see figure 6 and 7. Another source of differences might come from the interpolation errors in the low density region as seen in figures 3 and 4.

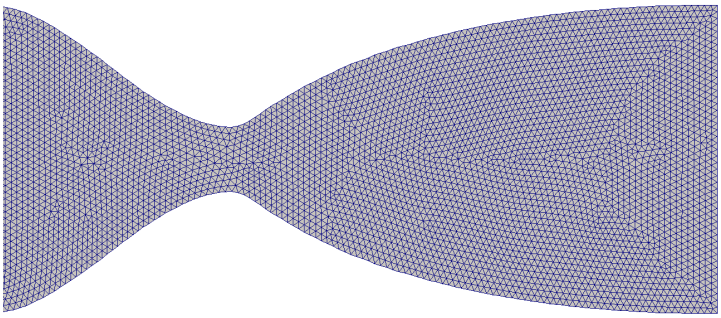

Figure 5: Picture of the unstructured triangular mesh

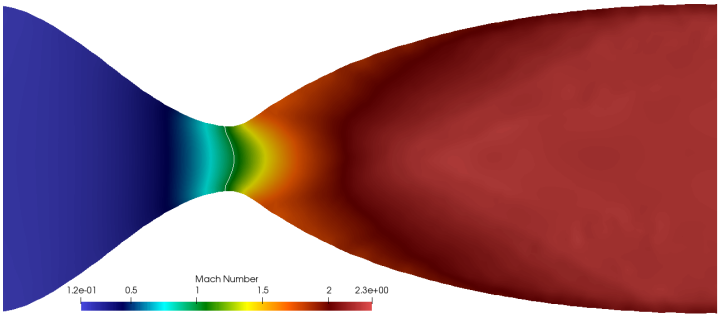

Figure 6: Mach number map with iso line of Mach=1

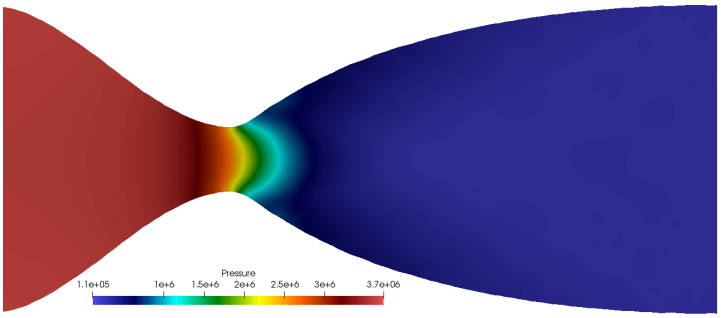

Figure 7: Pressure map

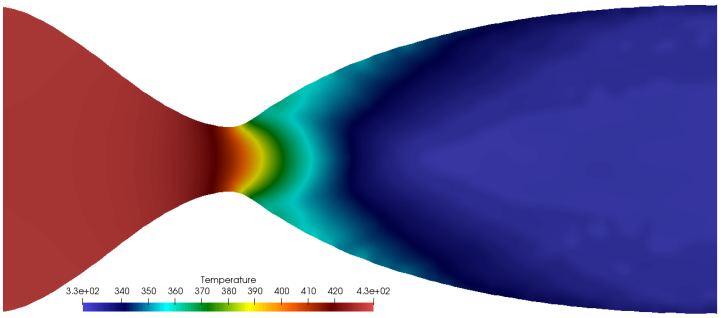

Figure 8: Temperature map

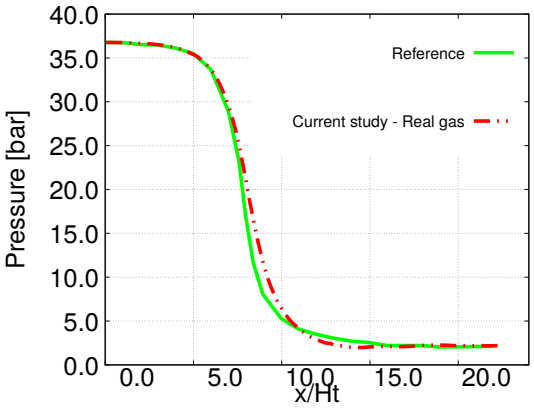

Figure 9: Pressure versus axial coordinate

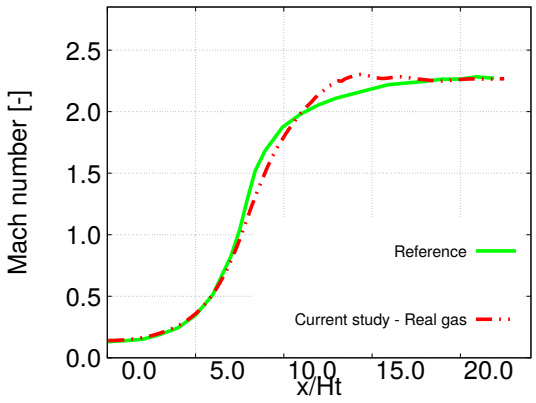

Figure 10: Mach number versus axial coordinate

9. CONCLUSIONS

In this study a finite volume solver with high order reconstruction is presented using look-up table interpolation to deal with real gas and multi optimal order detection to prevent numerical oscillations. The solver is tested on a supersonic R245fa nozzle expansion and show good behavior when comparing with available data. The modifications of the solver are not very intrusive, neither in terms of implementation nor in terms of performance. We believe, that this preliminary study open a lot of perspectives for the actual computation of turbomachinery operating with real gas.

REFERENCES

Bell, I. H., Wronski, J., Quoilin, S., and Lemort, V. (2014). Pure and Pseudo-pure Fluid Thermophysical Property Evaluation and the Open-Source Thermophysical Property Library CoolProp. *Industrial & Engineering Chemistry Research*, 53(6):2498–2508.

Clain, S., Diot, S., and Loubère, R. (2011). A high-order finite volume method for systems of conservation laws-Multi-dimensional Optimal Order Detection (MOOD). *Journal of Computational Physics*, 230(10):4028–4050.

Cueto-Felgueroso, L., Colominas, I., Fe, J., Navarrina, F., and Casteleiro, M. (2006). High-order finite volume schemes on unstructured grids using moving least-squares reconstruction. Application to shallow water dynamics. *International Journal for Numerical Methods in Engineering*, 65(3):295–331.

Cueto-Felgueroso, L., Colominas, I., Nogueira, X., Navarrina, F., and Casteleiro, M. (2007). Finite volume solvers and moving least-squares approximations for the compressible navier–stokes equations on unstructured grids. *Computer Methods in Applied Mechanics and Engineering*, 196(45):4712 – 4736.

Diot, S., Clain, S., and Loubère, R. (2012). Improved detection criteria for the Multi-dimensional Optimal Order Detection (MOOD) on unstructured meshes with very high-order polynomials. *Computers and Fluids*, 64:43–63.

Dumbser, M. and Diot, S. (2014). A New Family of High Order Unstructured MOOD and ADER Finite Volume Schemes for Multidimensional Sys- tems of Hyperbolic Conservation Laws.

Khelladi, S., Nogueira, X., Bakir, F., and Colominas, I. (2011). Toward a higher order unsteady finite

volume solver based on reproducing kernel methods. *Computer Methods in Applied Mechanics and Engineering*, 200(29-32):2348–2362.

Michalak, K. and Ollivier-Gooch, C. (2008). Limiters for unstructured higher-order accurate solutions of the Euler equations. *Proceedings of the AIAA forty-sixth ...*, pages 1–14.

Miyagawa, K. and Hill, P. G. (2002). Rapid and Accurate Calculation of Water and Steam Properties Using the Tabular Taylor Series Expansion Method. *Journal of Engineering for Gas Turbines and Power*, 123(3):707.

Nogueira, X., Colominas, I., Cueto-Felgueroso, L., and Khelladi, S. (2010). On the simulation of wave propagation with a higher-order finite volume scheme based on reproducing kernel methods. *Computer Methods in Applied Mechanics and Engineering*, 199(23):1471 – 1490.

Nogueira, X., Ramírez, L., Khelladi, S., Chassaing, J.-C., and Colominas, I. (2016). A high-order density-based finite volume method for the computation of all-speed flows. *Computer Methods in Applied Mechanics and Engineering*, 298:229 – 251.

Pini, M., Spinelli, a., Persico, G., and Rebay, S. (2015). Consistent look-up table interpolation method for real-gas flow simulations. *Computers & Fluids*, 107:178–188.

Rubino, A., Pini, M., Kosec, M., Vitale, S., and Colonna, P. (2018). A look-up table method based on unstructured grids and its application to non-ideal compressible fluid dynamic simulations. *Journal of Computational Science*, 28:70–77.

Sauret, E. and Gu, Y. (2014). Three-dimensional off-design numerical analysis of an organic Rankine cycle radial-inflow turbine. *Applied Energy*, 135:202–211.

Shima, E. and Kitamura, K. (2009). On new simple low-dissipation scheme of AUSM-family for all speeds. *AIAA paper*, (January):1–15.

Spinelli, A., Cammi, G., Zocca, M., Gallarini, S., Cozzi, F., Gaetani, P., Dossena, V., and Guardone, A. (2017). Experimental observation of non-ideal expanding flows of Siloxane MDM vapor for ORC applications. *Energy Procedia*, 129:1125–1132.

Spinelli, A., Pini, M., Dossena, V., Gaetani, P., and Casella, F. (2013). Design, Simulation, and Construction of a Test Rig for Organic Vapors. *Journal of Engineering for Gas Turbines and Power*, 135(4):042304.

Tartière, T. and Astolfi, M. (2017). A World Overview of the Organic Rankine Cycle Market. *Energy Procedia*, 129:2–9.

Tsoutsanis, P. (2018). Extended bounds limiter for high-order finite-volume schemes on unstructured meshes. *Journal of Computational Physics*, 362:69–94.

ACKNOWLEDGEMENT

Xesús Nogueira gratefully acknowledges the funding contributions of the Ministerio de Economía y Competitividad (grant # DPI2015-68431-R) of the Spanish Government and by the Consellería de Educación e Ordenación Universitaria of the Xunta de Galicia (grants # GRC2014/039 and # ED431C 2018/41), cofinanced with FEDER funds and the Universidade da Coruña..